Texture-Aware Ridgelet Transform and Machine Learning for Surface Roughness Prediction

Clayton Cooper[©], *Graduate Student Member, IEEE*, Jianjing Zhang[©], *Member, IEEE*, Liwen Hu[©], Yuebin Guo[©], and Robert X. Gao[©], *Fellow, IEEE*

Abstract-Quantification of machined surface roughness is critical to enabling estimation of part performance such as tribology and fatigue. As a contactless alternative to the traditional contact profilometry, photographic methods have been widely applied due to the advancement of image processing and ML techniques that allow the analysis of surface characteristics embedded in optical images and association of these characteristics with surface roughness. The state-of-the-art of photographic methods make extensive use of 2-D wavelet transform (WT) for image processing. However, a 2-D wavelet is often limited in capturing line patterns that are prevalent in the machined surface due to its radially symmetric nature, leading to suboptimal surface characterization. In addition, surface roughness prediction is primarily carried out as point prediction using ML methods which do not account for uncertainty in the models and data. To address these limitations, this study presents a ridgelet transform (RT)-based method for machined surface characterization. RT automatically detects the dominant line patterns, i.e., texture, in surface images and extracts topological features, such as the constituent spatial frequencies embedded in the surface profile along the direction that is most relevant for inducing surface roughness. The extracted texture-aware features are then used as inputs to random forest (RF) and kernel density estimation for surface roughness prediction and uncertainty quantification. Evaluation using experimental data shows that the developed method predicts surface roughness with an error of 0.5%, outperforming existing techniques and demonstrating the potential of RT as a viable technique for machined surface analysis.

Index Terms—ML, machining, prediction, random forest (RF), ridgelet, surface roughness, uncertainty analysis, wavelet.

Nomenclature

α Random forest input.β Random forest labels.

Manuscript received 30 July 2022; revised 5 September 2022; accepted 21 September 2022. Date of publication 13 October 2022; date of current version 2 November 2022. This work was supported by the U.S. National Science Foundation under Grant CMMI-2040288/2040358. The work of Clayton Cooper was supported by the National Science Foundation Graduate Research Fellowship under Grant 1937968. The Associate Editor coordinating the review process was Dr. Siliang Lu. (Clayton Cooper and Jianjing Zhang contributed equally to this work.) (Corresponding author: Robert X. Gao.)

Clayton Cooper, Jianjing Zhang, and Robert X. Gao are with the Department of Mechanical and Aerospace Engineering, Case Western Reserve University, Cleveland, OH 44106 USA (e-mail: cac197@case.edu; jxz170@case.edu; robert.gao@case.edu).

Liwen Hu and Yuebin Guo are with the Department of Mechanical and Aerospace Engineering, Rutgers University-New Brunswick, Piscataway, NJ 08854 USA, and also with the New Jersey Advanced Manufacturing Institute, Rutgers University-New Brunswick, New Brunswick, NJ 08854 USA (e-mail: lh660@scarletmail.rutgers.edu; yuebin.guo@rutgers.edu).

Digital Object Identifier 10.1109/TIM.2022.3214630

CNN Convolutional neural network.

 $\delta(\cdot)$ Dirac delta function.

DOC Depth of cut.
DT Decision tree.

 E_{energy} Ridgelet-extracted energy. E_{entropy} Ridgelet-extracted entropy.

f Surface roughness prediction model.

G Surface image.

GAF Gramian angular field. h Smoothing parameter of K. $k(\cdot)$ Kernel density estimate. $K(\cdot)$ Gaussian kernel function. l Stylus tracing length.

MAPE Mean absolute percentage error.

ML Machine learning.MLP Multi-layer perceptron.

 $P(\cdot)$ Scale power.

 p_m mth decision tree partition.

 $p(\cdot)$ Empirical PDF.

PDF Probability density function.

 $\psi(\cdot)$ Wavelet. $R(\cdot)$ Ridgelet.

Ra Arithmetic average roughness.Ra* Predicted surface roughness.

RF Random forest. $Rf(\cdot)$ Radon transform.

 ρ Directed distance from origin.

 $RT(\cdot)$ Ridgelet transform. s Wavelet scale parameter. STFT Short-time Fourier transform. SVM Support vector machine. τ Wavelet translation parameter.

 θ Angle about origin.

 θ^* Angle of machined surface texture.

v Measured surface profile. $WT(\cdot)$ Wavelet transform. x_i ith spatial coordinate.

I. Introduction

UMEROUS high-value components such as blisks and medical implants [1], [2] are fabricated using milling operations. Cutting-induced surface roughness at the microscopic scale (100–1000 nm) affects part properties and performance such as tribology, corrosion resistance, hydrodynamics, and electrical conductivity [3], [4], [5]. The behavior and

1557-9662 © 2022 IEEE. Personal use is permitted, but republication/redistribution requires IEEE permission. See https://www.ieee.org/publications/rights/index.html for more information.

service life of machined components can be predicted if their surface roughness is known, saving human and material resources throughout their life cycles.

Quantification of surface roughness has traditionally used contact profilometry, as illustrated in Fig. 1. A stylus is dragged along the surface to trace the surface profile, v, from which various roughness metrics can be calculated. However, contact profilometry has several limitations. It typically covers a small patch of material (<1 cm), is time consuming to execute (10-30 s), and requires expensive instruments [6], [7]. In response to these limitations, contactless *photographic* profilometry has become an attractive alternative due to the advancement of image processing and ML techniques over the past decades. These techniques allow for analyzing the optical surface images, extracting topological features that are relevant to surface characterization, and associating these features to surface roughness prediction [8]. Unlike other contactless methods, such as magnetic flux [9] and fringe projection [10], photographic methods require no equipment besides an optical microscope. In addition, photographs are taken in a fraction of a second, making real-time surface roughness prediction feasible [11]. Depending on the input to the predictive models used, techniques for photographic surface roughness prediction can be categorized into three groups: raw images, image statistical features, and wavelet coefficients.

Surface roughness prediction using *raw images* takes advantage of the image analysis capability provided by CNNs. CNN uses kernel-based convolution operations to extract local image features and assemble them from low-level to high-level, which are then associated with surface roughness prediction. Rifai et al. [12] used a CNN to process surface images directly and predicted surface roughness with 9% error. Wang et al. [13] improved upon this approach using a heterogenous CNN that considered tool wear as an additional model input when predicting roughness. The resulting surface roughness predictions had 4% error.

In contrast to raw image-based approaches, image statistical features have been explored to characterize a surface image or the discontinuity in the image using statistical features and relate them to the measured surface roughness. For example, Simunovic et al. [14] extracted the mean pixel value, standard deviation, and entropy from machined surface images, and then processed them by an adaptive neuro-fuzzy inference system to predict surface roughness, achieving a 7% error. In the work by Ghodrati et al. [15], surface discontinuities are first located using edge detection algorithms. Subsequently, the number of detected edges is associated with surface roughness using a linear model. It was found that the number of edges is correlated to surface roughness with a Pearson coefficient of 0.98. As another example, Prasad et al. [16] quantified the discontinuity of surface images using four statistics found from each image's gray-level co-occurrence matrix [17]. These statistics were used as inputs to a random forest (RF) model [18] which classified different levels of surface roughness with 6% error.

Recent studies on surface roughness prediction have increasingly investigated 2-D wavelet transform (WT) and achieved

state-of-the-art results. The 2-D WT describes the patterns of the constituent spatial frequencies in an image in terms of amplitude and location of their occurrences. Each spatial frequency describes the rate (cycles/pixel) at which an image oscillates between dark and light [19]. In photographic surface roughness quantification, oscillation is caused by the topological peaks and troughs as shown in of Fig. 1. As a result, wavelet coefficients that have the pattern of spatial frequencies encoded in them naturally characterize the surface image and can serve as the input to a surface roughness predictive model. For example, Morala-Argüello et al. [20] used the mean of 2-D wavelet coefficients as input to a MLP to predict the surface roughness of machined surfaces and achieved a 3% error. Similarly, Kamguem et al. [21] fused raw image statistics with 2-D wavelet statistics, e.g., wavelet response energy, to establish a total of six scalar surface roughness predictors. An MLP then used these features to predict surface roughness with 3% error.

Despite the progress, CNN and 2-D wavelet are not inherently suited for analyzing the direction of the lines or the surface profile in its perpendicular direction that is the most relevant for determining surface roughness. For example, the kernel in CNN only traverses in horizontal and vertical directions whereas kernel-based feature extraction is carried out only in squared image regions [22]. Also, 2-D wavelets are radially symmetric, making them suited for analyzing points rather than line patterns [19], [23]. As a result, surface characterization and surface roughness prediction based on CNN features or 2-D wavelet coefficients can lead to suboptimal outcomes.

To address these limitations, this study presents a textureaware surface roughness prediction method based on ridgelet transform (RT) [24], which has previously been investigated for image denoising [25], [26] and surface scratch extraction [27], [28]. Instead of having a radially symmetric shape, a ridgelet is a parameterized 2-D function that is constant along parallel lines while exhibiting a 1-D wavelet in the transverse direction. By leveraging the close relationship between the ridgelet and radon transform, the developed method can automatically detect the dominant line directions in the surface image and align the ridgelet in this direction. Then, by exploiting the scaling and translation parameters of the 1-D wavelet, the ridgelet can be adapted to different spatial frequencies embedded in the surface profile induced by peaks and valleys of the line patterns and extract their respective contribution to the formation of the surface topology as ridgelet coefficients by means of RT. To achieve optimal coefficient extraction, the measure of energy-to-entropy ratio is investigated for 1-D base wavelet selection to achieve the most compact representation of the surface spatial frequency bands. Subsequently, the powers of these bands are computed to serve as the input for ML-based surface roughness prediction and uncertainty quantification. A flowchart depicting the constituent components and their interactions of the developed method is shown in Fig. 2. The contributions of the presented study are summarized as follows:

1) Developed a texture-aware surface analysis method based on ridgelet that explicitly accounts for the line

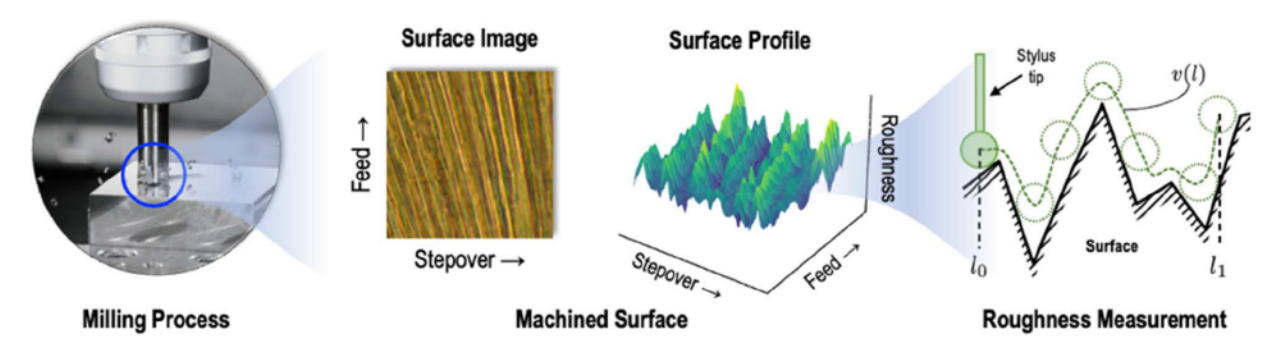


Fig. 1. Milling process and surface roughness measurement using contact profilometry.

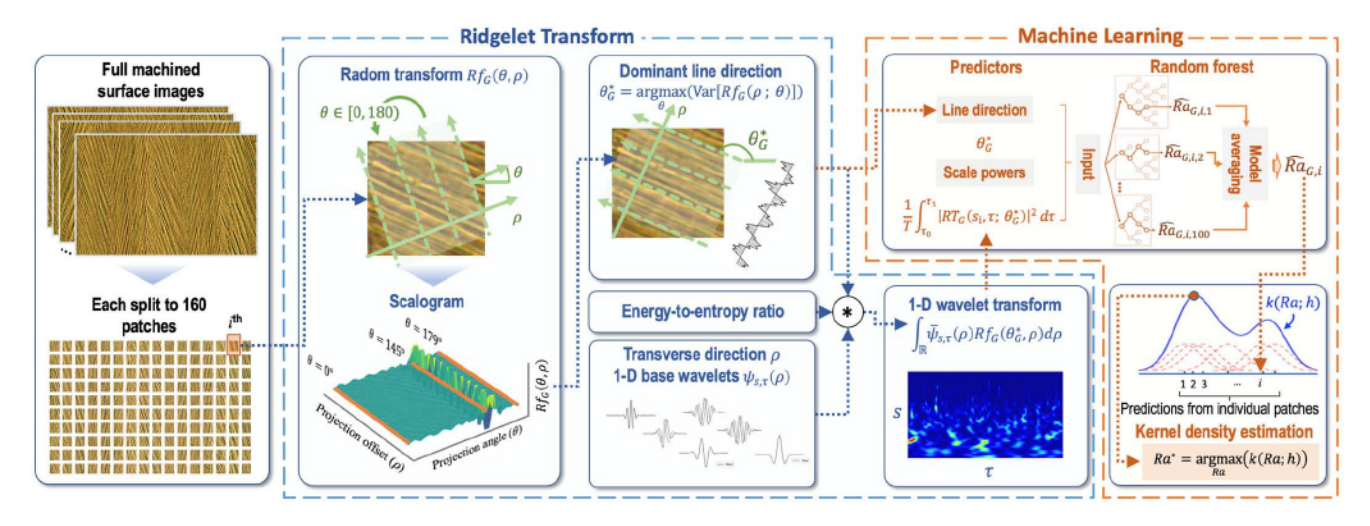


Fig. 2. Surface roughness prediction based on RT and ML.

patterns in machined surface images by automatically detecting the dominant line directions.

- 2) Extended the optimal 1-D base wavelet selection method to the context of ridgelet and designed new surface roughness predictors using the power of each RT spatial frequency based on the association between surface roughness and the amplitude of RT coefficients.
- Achieved improved surface roughness prediction accuracy as shown in the experimental evaluation through RF and kernel density estimation that considers uncertainty in both predictive model and data.

The rest of the article is organized as follows: Section II introduces the theoretical background of the RT, surface roughness prediction methodology based on RF, and kernel density estimation. Section III describes experiments performed to evaluate the developed method. Section IV discusses the results of the developed method on experimental data and compares it with the existing approaches to surface roughness prediction. Conclusions from this study and future research opportunities are presented in Section V.

II. THEORETICAL BACKGROUND AND METHODOLOGY

During milling, chips form at the end of each cutting tooth while the tooth is engaged with the workpiece. Each chip gouges the workpiece before it breaks off, inducing an oblique surface texture composed of parallel lines of ridges and valleys (Fig. 1) [29]. The most commonly used surface roughness

metric is the arithmetic average deviation from the centerline of the profile, Ra, defined in (1)

$$Ra = \frac{1}{l_1 - l_0} \int_{l_0}^{l_1} |v(l) - \bar{v}| dl \tag{1}$$

where l_0 and l_1 are the starting and stopping distances of the stylus used to trace the surface, and \bar{v} is the surface profile's mean value [29]. Because surface roughness is anisotropic, Ra is commonly found as Ra_{feed} and Ra_{step} in the feed and stepover directions, respectively, as shown in the coordinate system in Fig. 1. The objective of the presented study is to map the optical surface image to Ra via RT and ML that take into consideration the physical characteristics in milling surface texture and quantifies the uncertainty associated with the surface roughness prediction.

A. Ridgelet Transform

A ridgelet is a bivariate function over $\{x_1, x_2\} \in \mathbb{R}^2$ made by extruding a 1-D wavelet along a line. For a line $L_{\theta, \rho}$ in \mathbb{R}^2

$$L_{\theta,\rho}: x_1 \cos \theta + x_2 \sin \theta = \rho \tag{2}$$

and 1-D wavelet $\psi_{s,\tau}$

$$\psi_{s,\tau}(\rho) = \frac{1}{\sqrt{s}} \psi\left(\frac{\rho - \tau}{s}\right) \tag{3}$$

the corresponding ridgelet $R_{\theta,s,\tau}$ is

$$R_{\theta,s,\tau}(x) = \frac{1}{\sqrt{s}} \psi\left(\frac{x_1 \cos \theta + x_2 \sin \theta - \tau}{s}\right). \tag{4}$$

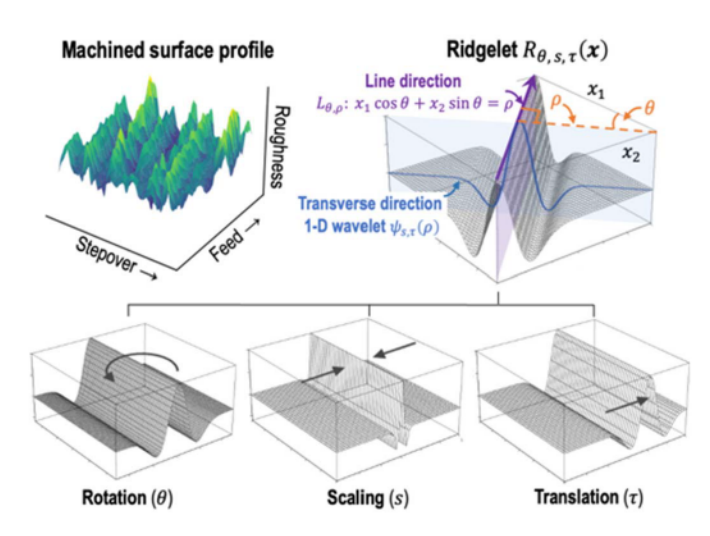


Fig. 3. Ridgelet and its properties for analyzing surface patterns.

In the above equations, θ is the angle between the line's normal vector (in the direction satisfying $0 \le \theta < \pi$) and x_1 , ρ is the directed distance between the line and origin, $\psi(\cdot)$ is a 1-D base wavelet, s > 0 is a scaling parameter that determines the wavelet's spatial frequency, $\tau \in \mathbb{R}$ is a translation parameter that shifts the wavelet [19], and $x = \{x_1, x_2\}$.

The ridgelet R is constant along the directions parallel to $L_{\theta,\rho}$ and is a 1-D wavelet $\psi_{s,\tau}(\rho)$ in the transverse direction. By adjusting the orientation parameter θ , scaling parameter s, and translation parameter τ , ridgelet R becomes adaptive to the possible variation of the line patterns on machined surface as shown in Fig. 3.

Consequently, characterizing different surfaces can be considered as determining the unique pattern with which each surface image can be decomposed into a combination of coefficients of 1-D wavelets with varying scales (spatial frequencies) and locations, in the direction perpendicular to the parallel lines. These coefficients are extracted through the convolution of the ridgelet and surface image G(x), known as the RT of G(x), defined in (5) [23]

$$RT_G(\theta, s, \tau) = \iint_{\mathbb{R}^2} \frac{1}{\sqrt{s}} \bar{\psi} \left(\frac{x_1 \cos \theta + x_2 \sin \theta - \tau}{s} \right) G(x) dx$$
(5)

where $\bar{\psi}$ is the conjugate of ψ .

Using the radon transform of G [30]

$$Rf_G(\theta, \rho) = \iint_{\mathbb{R}^2} G(x)\delta(\rho - x_1 \cos \theta - x_2 \sin \theta) dx \quad (6)$$

where δ is the dirac delta function, the RT of G in (5) can be reformulated as a 1-D WT in the transverse direction ρ (i.e., perpendicular to the line direction)

$$\begin{split} WT_{Rf}(s,\tau) &= \int_{\mathbb{R}} \bar{\psi}_{s,\tau}(\rho) Rf_G(\theta,\rho) d\rho \\ &= \int_{\mathbb{R}} \bar{\psi}_{s,\tau}(\rho) \bigg[\iint_{\mathbb{R}^2} G(x) \delta(\rho - x_1 \cos \theta - x_2 \sin \theta) dx \bigg] d\rho \\ &= \iint_{\mathbb{R}^2} \bigg[\int_{\mathbb{R}} \bar{\psi}_{s,\tau}(\rho) \delta(\rho - x_1 \cos \theta - x_2 \sin \theta) d\rho \bigg] G(x) dx \end{split}$$

$$= \iint_{\mathbb{R}^2} \frac{1}{\sqrt{s}} \bar{\psi} \left(\frac{x_1 \cos \theta + x_2 \sin \theta - \tau}{s} \right) G(x) dx$$

$$= RT_G(\theta, s, \tau). \tag{7}$$

The close connection between the Radon transform and the RT suggests that determining the line angle in the image can be achieved as an integral part of computing the RT_G . Only when the line integrals as represented by (6) are computed in the direction of the physical "ridges," θ_G^* , would the pixel values corresponding to the ridges and valleys accumulate, rather than canceling out each other. Consequently, the variance of $Rf_G(\rho;\theta)$ is maximized

$$\theta_G^* = \underset{\theta}{\operatorname{argmax}}(\operatorname{Var}[Rf_G(\rho; \theta)]). \tag{8}$$

Once θ_G^* is determined, surface characterization also requires that the ridgelet in the transverse direction matches the local spatial frequencies embedded in the surface profile. Therefore, the 1-D base wavelet selection should be optimized to capture the location and spatial frequencies information.

B. Selection of Base Wavelet

In this study, the measure of *energy-to-entropy* ratio is investigated to select the best 1-D base wavelet to define the ridgelet shape [31].

The information content of a signal can be considered as the total energy contained in the signal, expressed using the RT coefficients as

$$E_{\text{energy}} = \int_{-\infty}^{\infty} \int_{0}^{\infty} |RT_G(s, \tau; \theta_G^*)|^2 ds d\tau.$$
 (9)

Each RT coefficient that corresponds to a match between the base wavelet ψ and G in terms of angle, spatial frequency, and location will have a relatively high magnitude, and thus indicate effective information extraction.

In addition to extracting a high amount of information, the selected wavelet should also allow the coefficients to drop off quickly when a mismatch occurs, such that the surface profile can be compactly represented. Such "efficiency" in surface representation can be quantified using the Shannon entropy [32] (10), as shown at the bottom of the next page, where $p(\cdot)$ is the empirical PDF of $RT_G(s, \tau; \theta_G^*)$. The lower the entropy, the more compact the representation. As a result, the base wavelet corresponding to the highest energy-to-entropy ratio would yield the optimal surface profile characterization by considering both the information extraction and concentration in its representation.

In addition to the energy-to-entropy ratio, information theoretic measures such as mutual information and Kullback–Leibler (KL) divergence were also considered as candidate criterion for wavelet selection. The mutual information criterion [33] was proposed as part of an image denoising scheme using wavelets. The motivation was to remove white noise from a signal by picking a wavelet that maximizes the mutual information between the coefficients of the WT of the contaminated signal and the uncontaminated ground-truth signal. By assuming that the signal, noise, and wavelet coefficients were all normally distributed, mutual information was calculated in closed form and used as a wavelet selection

heuristic. The resulting scalogram contained a maximum level of information about the ground-truth signal, which could then be restored through inverse WT. In another study [34], KL divergence was proposed as a selection criterion wherein an ideal wavelet was sought for anomaly detection and classification in ultrasound images. To achieve minimum error in classification, a wavelet was chosen so that the KL divergence of wavelet coefficients between anomalous and normal classes was maximized. This maximized distance between the classes in wavelet space enabled accurate anomaly detection and classification.

Despite the successful applications, both information theoretic measures have limitations when characterizing surface profile in milling. On the one hand, mutual information only accounts for the energy aspect embedded in the energy-toentropy ratio measure. Specifically, by maximizing the mutual information between the signal (i.e., surface profile) and its wavelet coefficients, the selected base wavelet can only ensure that maximum information embedded in the signal is extracted using its wavelet representation. However, the regularity aspect of the surface profile induced by the milling process (such as alternative peaks and valleys across the whole surface image), as represented by the *entropy*, is not taken into consideration. Such regularity is reflected in a way that the surface profile can be decomposed into the combination of a small number of scaled and translated base wavelets. As a result, the energy concentration in the wavelet scalogram is expected to be sparse and drop off quickly when a mismatch between the base wavelet and the surface profile occurs, which is quantified as minimized *entropy* in the scalogram. On the other hand, while the measure of KL divergence is well suited for generating discriminative data features for the application of classification, it is not directly translatable to the application of regression (e.g., surface roughness prediction in the presented study), in which the output is a continuous variable as opposed to discrete classes to be separated.

C. Feature Extraction

RT with the appropriate base wavelet and line angle yields scalogram $RT_G(s,\tau;\theta_G^*)$, which consists of bands of varying spatial frequencies in the surface profile. The interactive effect among spatial frequencies determines surface roughness measured by means of a stylus. For example, high surface frequencies may overwhelm lower frequencies and cause small surface wavelengths, thus preventing the contact stylus from fully sinking into each valley as it moves along the surface to be profiled. Conversely, if high-frequency content is minimized, the traced profile will be more faithful to the true surface. Since photographic metrology is intended to replicate contact metrology, the related roughness prediction methods should consider these behaviors.

In this study, the spatial frequencies of the machined surface profile are represented using scale powers as

defined in (11)

$$P_G(s) = \frac{1}{\tau_1 - \tau_0} \int_{\tau_0}^{\tau_1} |RT_G(s, \tau; \theta_G^*)|^2 d\tau$$
 (11)

where τ_0 and τ_1 are the minimum and maximum τ values, respectively. Each scale power represents the mean amplitude of a specific spatial frequency on the surface.

D. RF for Surface Roughness Prediction

Although the scale powers encode the constituent spatial frequencies that form the surface topology, a quantitative relationship between these features and the surface roughness is yet to be determined. For this purpose, a data-driven predictive model that relates the scale powers with surface roughness is established in this study, which has the form of f

$$f(G) = f(P_G(s_1), P_G(s_2), \dots, P_G(s_N), \theta_G^*) = \widehat{Ra}_G$$
 (12)

it is noted that θ_G^* is included as an input such that the model is aware of the texture direction, and the anisotropy of the measurement can be explicitly considered when predicting the feed and stepover direction roughness.

In this study, a RF-based predictive model is developed, which is a supervised ensemble of binary DTs. In RF, each tree is formulated using a subset of the training data [18]. Specifically, each tree is trained by recursively partitioning the input feature space until each partitioned region (known as a "leaf") contains as few unique roughness values as possible, ideally only 1. Each partition is associated with a "decision rule," thus the name "DT." Once trained, the inference in each tree is performed for a given input by traversing the tree and heeding each decision rule until a leaf is reached. A RF prediction for a given input is then taken as the mean response of the trained tree ensemble to the same input.

Compared to other methods, a RF-based surface roughness prediction approach has two distinct advantages:

- 1) It uses a set of decision rules to map the inputs to surface roughness prediction, instead of relying on the computation between the input and model parameters such as weights in neural networks. As a result, it does not require data normalization and each input can differ in terms of the order of magnitude. This benefits the usage of scale power as model input as it can range over 5 orders of magnitude, for which the normalization process can induce numerical instability in computation and limit the model capability to generalize to unseen data
- 2) It simultaneously considers multiple possible models (as DTs) rather than betting on a single model. The advantage of such approach is the ability to quantify the uncertainty associated with the predictive model and obtain and fuse the information regarding the underlying association between scale powers and surface roughness

$$E_{\text{entropy}} = -\int_{-\infty}^{\infty} \int_{0}^{\infty} p(RT_G(s, \tau; \theta_G^*)) \log_2[p(RT_G(s, \tau; \theta_G^*))] ds d\tau$$
 (10)

from multiple models to improve not only the prediction accuracy, but also the robustness to variation in training data that individual models can suffer from.

Mathematically, given training input samples indexed by i, $\alpha_i = (P_G(s), \theta_G^*)_i \in \mathbb{R}^{N+1}$ and labeled training outputs $\beta_i = Ra_{G,i} \in \mathbb{R}^+$, the DT algorithm recursively partitions the feature space of α . For the m^{th} partition p_m , each candidate split of feature j at threshold t_m is evaluated, which partitions data into two disjoint subsets

$$p_m^{(1)} = \{(\alpha, \beta) \mid \alpha[j] \le t_m\}, \quad p_m^{(2)} = \{(\alpha, \beta) \mid \alpha[j] > t_m\}.$$
(13)

The effectiveness of the partition is then evaluated using a loss function computed from $p_m^{(1)}$ and $p_m^{(2)}$. In this study, the mean absolute percentage error, or MAPE, is evaluated [35]. MAPE describes the mean prediction error relative to the scale of the actual surface roughness values and is expressed as

MAPE =
$$\frac{1}{N} \sum_{i=1}^{N} \left| \frac{Ra_{G,i} - \widehat{Ra}_{G,i}}{Ra_{G,i}} \right|$$
 (14)

where $\widehat{Ra}_{G,i}$ denotes the surface roughness predicted by the DT algorithm for $\alpha_i \in p$, which is equal to the mean of $\beta_i \in p$. The loss function for the *m*th partition is expressed as sum of MAPEs computed using $p_m^{(1)}$ and $p_m^{(2)}$, weighted by the fraction of elements in each partition

$$L(j, t_m) = \frac{|p_m^{(1)}|}{|p_m^{(1)}| + |p_m^{(2)}|} \text{MAPE}(p_m^{(1)}) + \frac{|p_m^{(2)}|}{|p_m^{(1)}| + |p_m^{(2)}|} \text{MAPE}(p_m^{(2)}).$$
(15)

The optimal decision rule is obtained as the one with parameters j, t_m that lead to the minimization of (15)

$$j^*, t_m^* = \underset{i.t_m}{\operatorname{argmin}}(L(j, t_m)).$$
 (16)

The recursive splitting process continues until each partition contains only α_i that have the same corresponding β value [36]. Once trained, the results from individual trees in a forest allow for the evaluation of model uncertainty in surface roughness prediction, and the predicted roughness from the RF takes the mean of prediction results from all the DTs.

E. Data Uncertainty of Predicted Surface Roughness

Based on the texture-aware RT description, the algorithm requires that each surface image to be analyzed has only one dominant line direction such that the Radon transform can pinpoint the direction that is most relevant for inducing surface roughness. To facilitate such conformity for optimal surface roughness analysis, optical images of the machined surface are split into sub-image patches. The actual surface roughness reading of the surface is then the result of fusing the contribution (e.g., prediction result) from each patch. Depending on the locations in the original surface, the single-line angle patches over which the stylus directly passes would be better correlated with the surface roughness readings than those that are off the stylus trajectory or have multiple line

Algorithm 1 Surface Image Processing and Roughness Prediction

Input: surface image set G; candidate wavelet set, ψ **Output:** surface roughness predictions, Ra^*

- 1 for each G in G:
- 2 Find θ_G^* using (8)
- 3 Calculate energy-to-entropy ratio of candidate wavelets on texture-aligned surface profile using (9) and (10)
- 4 end for
- 5 Determine best wavelet (highest average energy-to-entropy ratio)
- 6 **for each** *G* in *G*:
- 7 Calculate scale powers using (11)
- 8 Make (α, β) tuple for G
- 9 end for
- 10 Train random forest of N decision trees using (16)
- 11 Estimate PDF of each machined surface using (17)
- 12 **return** Ra^* for each surface using G and (19)

angles. Consequently, prediction results from each image patch can be considered as representing a probability distribution that is inherent to the surface roughness data. The surface roughness that corresponds to the highest probability indicates the most probable roughness value of the whole machined surface, obtained through fusion of all patches.

To estimate the PDF of the predicted surface roughness distribution, the method of kernel density estimation is investigated [37]. The basic idea is to allocate higher probability density to the locations where surface roughness predictions are more clustered (which are expected from patches with a single dominant line angle) than the locations where predictions are less clustered (which are expected from patches with varying mixture of line angles). For a total of n surface roughness predictions from (12): $\widehat{Ra}_{G,i}$, i = 1, 2, ..., n, the density estimate, k, is expressed as

$$k(Ra; h) = \frac{1}{nh} \sum_{i=1}^{n} K\left(\frac{Ra - \widehat{Ra}_{G,i}}{h}\right) \tag{17}$$

where K is a Gaussian kernel function such that

$$k(Ra; h) \propto \exp\left(-\frac{Ra^2}{2h^2}\right)$$
 (18)

and h is a smoothing parameter. The higher the h, the smoother the PDF. Once the PDF is determined using (17), the final surface roughness prediction can be obtained as

$$Ra^* = \underset{Ra}{\operatorname{argmax}}(k(Ra; h)). \tag{19}$$

A pseudocode summary of the proposed signal processing and ML methods is shown in Algorithm 1.

III. EXPERIMENTAL EVALUATION

To evaluate the effectiveness of the developed method, hardened AISI H13 tool steel (50 ± 1 HRC) was machined under dry conditions on a CNC mill using a two-flute, 20 mm diameter end mill equipped with (Ti, Al)N/TiN coated tungsten

TABLE I
MACHINING PARAMETERS AND SURFACE ROUGHNESS

G	Speed (mm/min)	Feed/tooth (mm/tooth)	Radial DOC (mm)	Ra _{step} (nm)	Ra _{feed} (nm)
1	200	0.1	0.3	241	87
2	200	0.1	0.5	520	372
3	200	0.1	0.5	384	105
4	200	0.05	0.5	360	83
5	200	0.1	0.4	646	145
6	100	0.1	0.5	440	216
7	200	0.1	0.5	480	118
8	300	0.1	0.5	650	75
9	200	0.05	0.5	372	116
10	200	0.1	0.4	329	116
11	100	0.1	0.5	399	133
12	300	0.1	0.5	396	111
13	200	0.1	0.3	426	137
14	200	0.05	0.5	374	78
15	200	0.2	0.5	488	134
16	100	0.1	0.5	356	191
17	200	0.1	0.3	265	158
18	200	0.1	0.4	399	151
19	200	0.2	0.3	584	241
20	300	0.1	0.5	657	79
21	200	0.2	0.5	1059	380

carbide inserts. Each workpiece measured $100 \times 20 \times 12$ mm and each linear cut removed a 1 mm thick layer from the 100×20 mm face. A total of 21 samples were machined at varying speeds, feeds per tooth, and radial DOC. The experimental design with the machining parameters and the resulting Ra values found through contact profilometry are shown in Table I.

For photographic profilometry, a 1600×1000 px image (G) was taken of each machined surface using an optical microscope, with 1 image pixel corresponding to a surface region of size $2 \times 2 \mu m$. Each image was then broken into 160 non-overlapping image patches g of size 100×100 px. In total, 3360 image patches are generated, which are then split into a training and a testing dataset with a split ratio of 67–33 (i.e., 2240 image patches for the training dataset, 1120 image patches for the testing dataset).

For image processing using RT, the dominant line angles are first determined for each image patch using (8), and the increment of angle θ in performing the radon transform is 1°. To evaluate the performance of the 1-D base wavelet in terms of information extraction, the energy-to-entropy ratio is evaluated on seven wavelet families with training data: complex Gaussian, complex Morlet, frequency B-spline, Gaussian, Morlet, Ricker, and Shannon, representing some of the most investigated 1-D base wavelets in signal processing. In Table II, representative wavelets and their respective expressions and energy-to-entropy ratios are tabulated. As a result, the Ricker wavelet is chosen as it had the highest ratio of all the wavelets investigated. The scale parameter of 1-D wavelet follows 2^{-3} , $2^{-2.875}$, ..., 2^3 .

To correlate the scale powers from the RT with surface roughness, two RF models were trained to predict Ra_{step} and Ra_{feed} , respectively. Each model had 100 DTs and each tree was trained on a set of 2240 image patches from the training dataset, sampled with replacement. Each tree was fit to its training data until it exhibited 0% MAPE. The smoothing parameter h in the kernel density estimation to extract the PDF of the predicted surface roughness distribution is set to 15 through cross-validation.

IV. RESULTS AND DISCUSSION

The performance of the developed surface roughness prediction method is illustrated and compared with several existing techniques.

A. Surface Roughness Predictive Accuracy

The trained RF models were used to predict the surface roughness in the feed and stepover directions (Fig. 1) for the testing dataset. Specifically, the image patches from a machined surface were fed into the model to obtain the individual predictions $\widehat{Ra}_{G,i}$. Subsequently, these individual predictions are fused using kernel density estimation to obtain the PDF of surface roughness prediction. The final surface roughness prediction is determined using (19).

The scatterplots of the surface roughness prediction in the feed and stepover directions are shown in Fig. 4. The horizontal axes represent the predicted surface roughness results, whereas the vertical axes denote the measured surface roughness values. The 45° line indicates the perfect prediction. It is noted that predicted results as reflected in the dots/triangles are closely aligned with the ideal line, indicating good performance. To obtain quantitative evaluation, both the MAPE and the coefficient of determination R^2 are computed. The R^2 specifically reflects on the proportion of the variance in the data that is explained by the predictors in the RF model, namely, the scale powers and the dominant line angle. The developed method achieved MAPE of 0.5% and R^2 of 0.99 in surface roughness prediction in both feed and stepover directions, demonstrating good performance.

The inset of Fig. 4 shows the mean prediction errors of RF over all the testing samples as compared to the mean prediction errors that would have been achieved using individual DTs in the forest. The vertical axis is expressed in log-scale. It is seen that by fusing the prediction results from all the 100 trees, the predictive errors are significantly reduced. Quantitatively, the mean prediction error is reduced from 38 to 0.5 nm for Ra_{feed} and from 59 to 0.7 nm for Ra_{step} . This indicates that through data fusion, ensemble-based methods such as RF, can be effective in reducing the variability in surface texture and the uncertainty regarding the underlying association between the texture and roughness.

Fig. 5 shows comparison of surface roughness prediction performance quantified by MAPE among the developed method (RT + RF), four alternative surface roughness prediction models (SVM, MLP, CNN, and DT), and three alternative signal processing methods (STFT, GAF, and WT) for the surface profile. The SVM, MLP, DT, and RF models

Complex Complex Frequency B-Ricker Gaussian n Morlet Shannon Gaussian n Morlet Spline Plot $e^{i2\pi t}$ $\psi(t) \propto e^{-t^2/2} \cos(\omega t) \psi(t) \propto e^{-t^2/2} (1$ $\psi(t) \propto \frac{d^n}{dt^n}e^{-t}$ E/E ratio $4.72 \sim 8.13$ 7.54 4.09 $4.97 \sim 8.02$ 7.96 9.12 7.12 $(\times 10^9)$

TABLE II
1-D BASE WAVELET CANDIDATES AND COMPARISON OF ENERGY-TO-ENTROPY RATIO

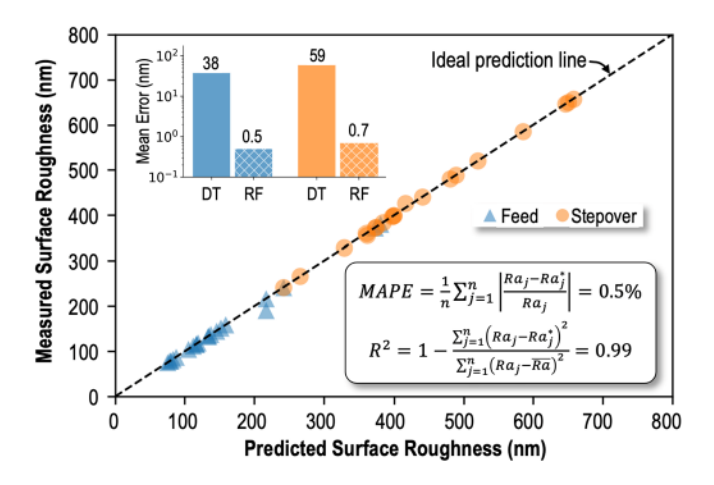


Fig. 4. Scatterplots of roughness predictions using developed method (DT: decision tree, RF: RF).

each predicted surface roughness using scale powers of the specified transform whereas the CNN predicted roughness using the surface images directly. It is seen that the method of RT + RF exhibits the lowest MAPE as well as the smallest uncertainty amongst the techniques investigated. Interestingly, by replacing the ensemble method RF with non-ensemble SVM, MLP, or DT, the prediction error in MAPE is shown to have increased by 4–16 times (from 0.5% to over 2.0% for DT and from 0.5% to over 8.0% for SVM). This shows that by relying on a single predictive model rather than fusing results from multiple possible models as in RF, the expected prediction error can increase significantly, which confirms the trend as shown in the inset of Fig. 4.

B. Prediction Uncertainty as PDF of Surface Roughness

To evaluate the surface roughness prediction performance and quantify prediction uncertainty, the PDFs of the prediction from individual patches in the feed direction for workpiece #2 and in the stepover direction for workpiece #21 are plotted in Fig. 6(a) and (b), respectively. The PDFs are obtained through kernel density estimation and the raw prediction results from individual patches are shown as dots below the PDF curve. It is noted that both PDFs contain a dominant peak along with several smaller peaks on the side as prediction outliers.

To further investigate the prediction under these peaks, four sample image patches corresponding to the individual

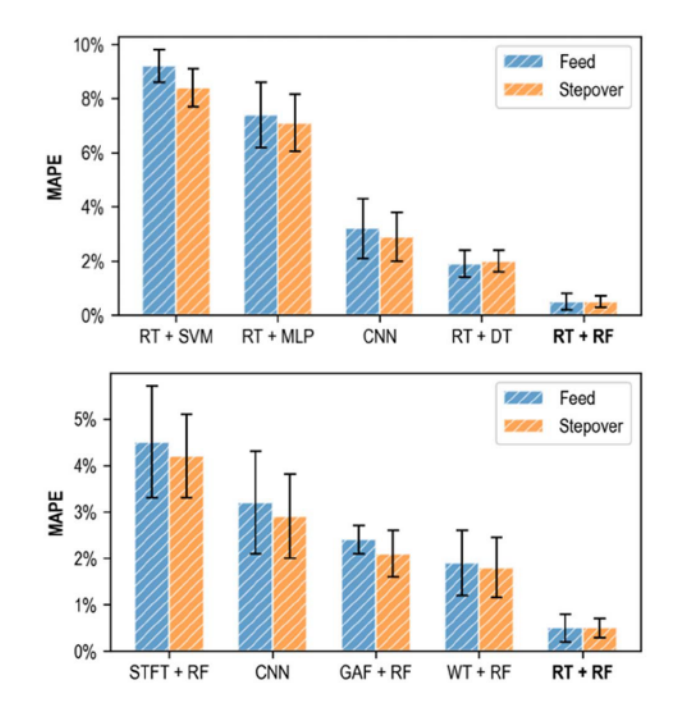


Fig. 5. Performance comparison of surface roughness prediction when RT is chosen as the signal processing model (top) and RF is chosen as the prediction model (bottom). RT + RF consistently produces the lowest error as compared to the other techniques, indicating the advantages of the proposed method in surface roughness prediction. (RT: ridgelet transform, SVM: support vector machine, MLP: multi-layer perceptron, CNN: convolutional neural network, DT: decision tree, RT: ridgelet transform, RF: RF, STFT: short-time Fourier transform, GAF: Gramian angular field).

prediction results are shown to the left of the PDFs in Fig. 6. The locations of these patches in the original surface images are illustrated on the right. It is seen that the results under the main peak of the PDF all come from the image patches where there is a single dominant line direction (e.g., ① and ②), while the results under the smaller peaks come from the image patches with the presence of multiple texture angles (e.g., ③ and ④).

These angles are induced by *scalloping*, a process characteristic of milling wherein the surface texture differs between adjacent parallel cuts due to the cutter stepover, which is equivalent to the radial depth of cut. The texture between stepover regions, annotated in Fig. 6 is induced by the endmill's diametric edges whereas the texture within the stepover region

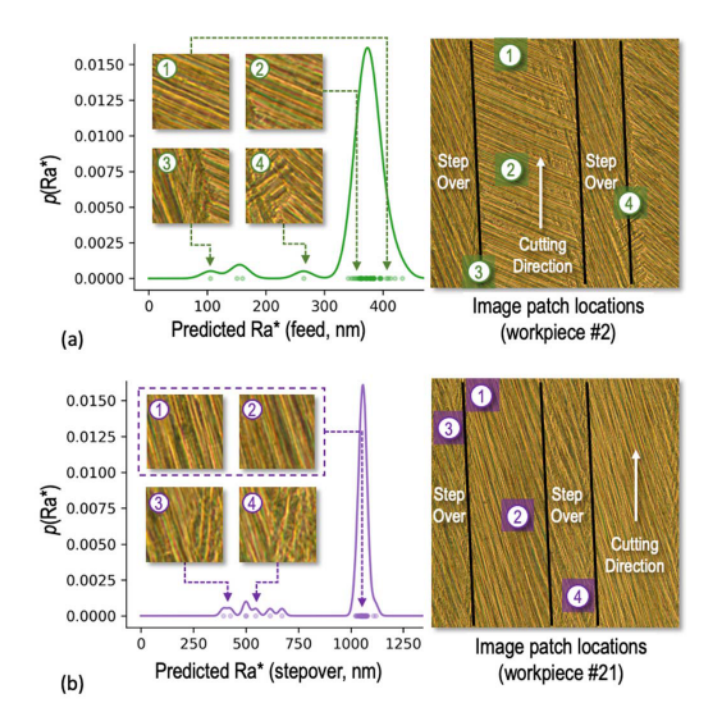


Fig. 6. PDF of surface roughness prediction from kernel density estimation and corresponding locations of image patches. (a) Surface roughness prediction in feed direction. (b) Surface roughness prediction in stepover direction.

is induced by the endmill's bottom edges. Chip formation dynamics and rake angles differ between these cutting edges, causing the intersecting surface textures to differ and become nonparallel.

It is seen from Fig. 6 that the developed methods based on RT and RF can provide consistent prediction for the image patches that are within the uniform region, as reflected by the narrow peaks in the PDFs. In addition, it demonstrated the effectiveness of kernel density estimation in effectively fusing these "inline" predictions while being robust to the outlier predictions, induced by image patches containing mixture of line angles, in producing the final surface roughness prediction.

V. Conclusion

To advance the state of research in photographic profilometry for contactless characterization and roughness prediction of machined surfaces, a texture-aware method based on RT and ML has been developed. The rotation, translation, and scaling properties of ridgelets allow for tailored surface characterization in terms of matching the dominant surface line directions as well as the varying spatial frequencies of the surface profile. The measure of energy-to-entropy ratio is then investigated to optimize surface feature extraction as ridgelet coefficients. Taking the powers of the extracted features at different spatial frequency bands as input, the PDF of the surface roughness is obtained using RF and kernel density estimation, enabling final roughness prediction and uncertainty quantification. Experimental evaluation on machined H13 tool steel showed that the developed method achieves a surface roughness prediction mean absolute percentage error of 0.5% and a prediction R^2 value of 0.99, in both the feed and stepover directions. These results outperform the existing methods based on 2-D WT and CNNs and indicate ridgelet as an effective image processing

approach for machined surface analysis. Future research will extend the ridgelet-based method for surface characterization of other manufacturing processes. Also, research will be directed toward understanding uncertainty involved in surface roughness prediction to further improve the accuracy and robustness of the developed predictive method.

REFERENCES

- P. Gilge, A. Kellersmann, J. Friedrichs, and J. R. Seume, "Surface roughness of real operationally used compressor blade and blisk," *Proc. Inst. Mech. Eng.*, G, J. Aerosp. Eng., vol. 233, no. 14, pp. 5321–5330, Nov. 2019, doi: 10.1177/0954410019843438.
- [2] A. I. Nicolas-Silvente, E. Velasco-Ortega, I. Ortiz-Garcia, L. Monsalve-Guil, J. Gil, and A. Jimenez-Guerra, "Influence of the titanium implant surface treatment on the surface roughness and chemical composition," *Materials*, vol. 13, no. 2, p. 314, Jan. 2020, doi: 10.3390/ma13020314.
- [3] B. Zhao, J. Song, L. Xie, Z. Hu, and J. Chen, "Surface roughness effect on fatigue strength of aluminum alloy using revised stress field intensity approach," *Sci. Rep.*, vol. 11, no. 1, p. 19279, Dec. 2021, doi: 10.1038/s41598-021-98858-0.
- [4] X. Gu and F. Cegla, "The effect of internal pipe wall roughness on the accuracy of clamp-on ultrasonic flowmeters," *IEEE Trans. Instrum. Meas.*, vol. 68, no. 1, pp. 65–72, Jan. 2019, doi: 10.1109/TIM.2018.2834118.
- [5] F. Capelli, J.-R. Riba, E. Ruperez, and J. Sanllehi, "A genetic-algorithm-optimized fractal model to predict the constriction resistance from surface roughness measurements," *IEEE Trans. Instrum. Meas.*, vol. 66, no. 9, pp. 2437–2447, Sep. 2017, doi: 10.1109/TIM.2017.2707938.
- [6] T. Jeyapoovan and M. Murugan, "Surface roughness classification using image processing," *Measurement*, vol. 46, no. 7, pp. 2065–2072, Aug. 2013, doi: 10.1016/j.measurement.2013.03.014.
- [7] Quick Guide to Surface Roughness Measurement, Mitutoyo, Aurora, IL, USA, Dec. 2016.
- [8] Y. Liu, L. Guo, H. Gao, Z. You, Y. Ye, and B. Zhang, "Machine vision based condition monitoring and fault diagnosis of machine tools using information from machined surface texture: A review," *Mech. Syst. Signal Process.*, vol. 164, Feb. 2022, Art. no. 108068, doi: 10.1016/j.ymssp.2021.108068.
- [9] E. Li, J. Wang, J. Wu, and Y. Kang, "Spatial-spectrum-based measurement of the surface roughness of ferromagnetic components using magnetic flux leakage method," *IEEE Trans. Instrum. Meas.*, vol. 70, pp. 1–10, 2021, doi: 10.1109/TIM.2020.3031171.
- [10] X. Pei, J. Liu, Y. Yang, M. Ren, and L. Zhu, "Phase-to-coordinates calibration for fringe projection profilometry using Gaussian process regression," *IEEE Trans. Instrum. Meas.*, vol. 71, pp. 1–12, 2022, doi: 10.1109/TIM.2022.3162275.
- [11] S. K. Everton, M. Hirsch, P. Stravroulakis, R. K. Leach, and A. T. Clare, "Review of in-situ process monitoring and in-situ metrology for metal additive manufacturing," *Mater. Des.*, vol. 95, pp. 431–445, Apr. 2016, doi: 10.1016/j.matdes.2016.01.099.
- [12] A. P. Rifai, H. Aoyama, N. H. Tho, S. Z. Md Dawal, and N. A. Masruroh, "Evaluation of turned and milled surfaces roughness using convolutional neural network," *Measurement*, vol. 161, Sep. 2020, Art. no. 107860, doi: 10.1016/j.measurement.2020.107860.
- [13] P. Wang, Z. Liu, R. X. Gao, and Y. Guo, "Heterogeneous data-driven hybrid machine learning for tool condition prognosis," CIRP Ann., vol. 68, no. 1, pp. 455–458, 2019, doi: 10.1016/j.cirp.2019.03.007.
- [14] G. Simunovic, I. Svalina, K. Simunovic, T. Saric, S. Havrlisan, and D. Vukelic, "Surface roughness assessing based on digital image features," Adv. Prod. Eng. Manage., vol. 11, no. 2, pp. 93–104, May 2016, doi: 10.14743/apem2016.2.212.
- [15] S. Ghodrati, M. Mohseni, and S. G. Kandi, "Application of image edge detection methods for precise estimation of the standard surface roughness parameters: Polypropylene/ethylene-propylene-dienemonomer blend as a case study," *Measurement*, vol. 138, pp. 80–90, May 2019, doi: 10.1016/j.measurement.2019.02.033.
- [16] G. Prasad, G. S. Vijay, and R. Kamath C., "Comparative study on classification of machined surfaces using ML techniques applied to GLCM based image features," *Mater. Today, Proc.*, vol. 62, pp. 1440–1445, 2022, doi: 10.1016/j.matpr.2022.01.285.
- [17] B. Sebastian V, A. Unnikrishnan, and K. Balakrishnan, "Gray level co-occurrence matrices: Generalisation and some new features," 2012, arXiv:1205.4831.

- [18] L. Breiman, "Random forests," Mach. Learn., vol. 45, no. 1, pp. 5–32, 2001, doi: 10.1023/A:1010933404324.
- [19] R. X. Gao and R. Yan, Wavelets: Theory and Applications for Manufacturing. Boston, MA, USA: Springer, 2011, doi: 10.1007/978-1-4419-1545-0.
- [20] P. Morala-Argüello, J. Barreiro, and E. Alegre, "A evaluation of surface roughness classes by computer vision using wavelet transform in the frequency domain," *Int. J. Adv. Manuf. Technol.*, vol. 59, nos. 1–4, pp. 213–220, Mar. 2012, doi: 10.1007/s00170-011-3480-6.
- [21] R. Kamguem, A. S. Tahan, and V. Songmene, "Surface roughness estimation of turned parts from optical image measurements and wavelet decomposition," *Int. J. Mater. Forming Machining Processes*, vol. 1, no. 1, pp. 48–72, Jan. 2014, doi: 10.4018/ijmfmp.2014010104.
- [22] Y. LeCun, Y. Bengio, and G. E. Hinton, "Deep learning," Nature, vol. 521, pp. 436–444, May 2015, doi: 10.1038/nature14539.
- [23] E. J. Candes, RIDGELETS: Theory and Applications. Stanford, CA, USA: Stanford Univ., 1998.
- [24] E. J. Candès and D. L. Donoho, "Ridgelets: A key to higher-dimensional intermittency?" Philos. Trans. Roy. Soc. London A, Math. Phys. Sci., vol. 357, no. 1760, pp. 2495–2509, Sep. 1999, doi: 10.1098/rsta.1999.0444.
- [25] B. Zhang, J. M. Fadili, and J.-L. Starck, "Wavelets, ridgelets, and curvelets for Poisson noise removal," *IEEE Trans. Image Process.*, vol. 17, no. 7, pp. 1093–1108, Jul. 2008, doi: 10.1109/TIP.2008.924386.
- [26] G. Y. Chen and B. Kégl, "Image denoising with complex ridgelets," Pattern Recognit., vol. 40, no. 2, pp. 578–585, Feb. 2007, doi: 10.1016/j.patcog.2006.04.039.
- [27] X. Jiang, W. Zeng, P. Scott, J. Ma, and L. Blunt, "Linear feature extraction based on complex ridgelet transform," Wear, vol. 264, nos. 5–6, pp. 428–433, Mar. 2008, doi: 10.1016/j.wear.2006.08.040.
- [28] J. Ma, X. Jiang, and P. Scott, "Complex ridgelets for shift invariant characterization of surface topography with line singularities," *Phys. Lett. A*, vol. 344, no. 6, pp. 423–431, Sep. 2005, doi: 10.1016/j.physleta.2005.06.091.
- [29] E. Oberg, F. D. Jones, H. L. Horton, H. H. Ryffel, C. J. McCauley, and L. Brengelman, *Machinery's Handbook*, 31st ed. South Norwalk, CT, USA: Industrial Press, Inc, 2020.
- [30] J. Radon, "On the determination of functions from their integral values along certain manifolds," *IEEE Trans. Med. Imag.*, vol. MI-5, no. 4, pp. 170–176, Dec. 1986, doi: 10.1109/TMI.1986.4307775.
- [31] R. Yan and R. X. Gao, "Base wavelet selection for bearing vibration signal analysis," *Int. J. Wavelets, Multiresolution Inf. Process.*, vol. 7, no. 4, pp. 411–426, Jul. 2009, doi: 10.1142/S0219691309002994.
- [32] C. E. Shannon, "A mathematical theory of communication," Bell Syst. Tech. J., vol. 27, no. 3, pp. 379–423, Jul. 1948, doi: 10.1002/j.1538-7305.1948.tb01338.x.
- [33] L. Zhang, P. Bao, and X. Wu, "Multiscale LMMSE-based image denoising with optimal wavelet selection," *IEEE Trans. Circuits Syst. Video Technol.*, vol. 15, no. 4, pp. 469–481, Apr. 2005, doi: 10.1109/TCSVT.2005.844456.
- [34] P. P. C. Tsui and O. A. Basir, "Wavelet basis selection and feature extraction for shift invariant ultrasound foreign body classification," *Ultrasonics*, vol. 45, nos. 1–4, pp. 1–14, Dec. 2006, doi: 10.1016/j.ultras.2006.05.214.
- [35] B. Malakooti, Operations and Production Systems With Multiple Objectives. Hoboken, NJ, USA: Wiley, 2014.
- [36] M. R. Segal, "Machine learning benchmarks and random forest regression," Center Bioinf. Mol. Biostatist., Univ. California, San Francisco, CA, USA, Tech. Rep., Apr. 2004. [Online]. Available: https://escholarship.org/uc/item/35x3v9t4
- [37] Y. Chen, "A tutorial on kernel density estimation and recent advances," *Biostatist. Epidemiol.*, vol. 1, no. 1, pp. 161–187, Jan. 2017, doi: 10.1080/24709360.2017.1396742.



Clayton Cooper (Graduate Student Member, IEEE) received the B.S. and M.S. degrees in mechanical engineering from Case Western Reserve University, Cleveland, OH, USA, in 2020, where he is currently pursuing the Ph.D. degree in mechanical engineering.

He is a 2020 NSF Graduate Research Fellow. He is currently as a Research Assistant with Case Western Reserve University. His research interests include physics-informed machine learning, process optimization, and predictive metrology.



Jianjing Zhang (Member, IEEE) received the Ph.D. degree in mechanical engineering from Case Western Reserve University, Cleveland, OH, USA. in 2022.

He is currently a Post-Doctoral Research Associate with Case Western Reserve University. His research interests include physics-informed machine learning and uncertainty quantification for modeling of cyber physical systems and human–robot collaboration in smart manufacturing.



Liwen Hu received the M.S. degree in mechanical engineering from Missouri University of Science and Technology, Rolla, MO, USA, in 2017. He is currently pursuing the Ph.D. degree in mechanical engineering with Rutgers University, New Brunswick, NJ, USA.

His research focuses on physics-informed machine learning and optimization of manufacturing processes.



Yuebin Guo is the Henry Rutgers Professor of Advanced Manufacturing at Rutgers University–New Brunswick, New Brunswick, NJ, USA. His research interests are in AI for manufacturing, digital twin, physics-informed machine learning, and materials informatics. He is the author of more than 300 peer-refereed technical publications in these areas and an Elected Fellow of ASME, SME, and CIRP.

Prof. Guo was a recipient of numerous awards, including the SME Albert M. Sargent Progress

Award, ASME Federal Government Swanson Fellowship, NSF CAREER, and SME Outstanding Young Manufacturing Engineer.



Robert X. Gao (Fellow, IEEE) receiving the Ph.D. degree from the Technical University of Berlin, Berlin, Germany, in 1991.

He is the Cady Staley Professor of Engineering and the Chair of the Department of Mechanical and Aerospace Engineering, Case Western Reserve University, Cleveland, OH, USA. He has been working on multiphysics sensing, stochastic modeling, AI, and physics-informed machine learning for improving the observability of cyber physical systems. He has published three books and over 400 refereed

papers, including more than 190 journal articles. He is a fellow of ASME, SME, and CIRP.

Dr. Gao was a recipient of the SME Eli Whitney Productivity Award, the ASME Blackall Machine Tool and Gage Award, the IEEE Instrumentation and Measurement Society Technical Award, the IEEE Best Application in Instrumentation and Measurement Award, the NSF Early CAREER Award, and several best paper awards. He was a Distinguished Lecturer of the IEEE Instrumentation and Measurement Society and the IEEE Electron Devices Society. He is currently serving as a Senior Editor for the IEEE/ASME TRANSACTIONS ON MECHATRONICS.